Eur. Phys. J. C (2022) 82:719
https://doi.org/10.1140/epjc/s10052-022-10676-4

THE EUROPEAN PHYSICAL JOURNAL C

Regular Article - Theoretical Physics

Medium modification of the nucleon mechanical properties: Abel tomography case

June-Young Kim[1,a], **Ulugbek Yakhshiev**[2,3,b], **Hyun-Chul Kim**[2,4,c]

[1] Fakultät für Physik und Astronomie, Institut für Theoretische Physik II, Ruhr-Universität Bochum, 44780 Bochum, Germany
[2] Department of Physics, Inha University, Incheon 22212, Republic of Korea
[3] Theoretical Physics Department, National University of Uzbekistan, 100174 Tashkent, Uzbekistan
[4] School of Physics, Korea Institute for Advanced Study (KIAS), Seoul 02455, Republic of Korea

Received: 5 July 2022 / Accepted: 3 August 2022 / Published online: 18 August 2022

Abstract We investigate how the gravitational form factors of the nucleon undergo changes in nuclear matter, emphasizing the Abel transformation from the three-dimensional (3D) Breit frame to the two-dimensional (2D) light-front frame. Since the gravitational form factors reveal the mechanical structure of the nucleon, we examine also the medium modifications of the energy–momentum, pressure, and shear-force distributions. We scrutinize the stabilities of the nucleon in nuclear matter. For this purpose, we employ the in-medium modified SU(2) Skyrme model to study these mechanical quantities of the nucleon, since it provides a simple but clear framework. In this in-medium modified SU(2) Skyrme model, the modification of pionic properties is performed by using low-energy pion-nucleus scattering data and the saturation properties of nuclear matter near the normal nuclear matter density, $\rho_0 = 0.5 m_\pi^3$. The results reveal how the nucleon swells in nuclear matter as the mass distribution of the nucleon is broadened in medium. We also show that the mean square radii corresponding to the mass and angular momentum distributions increase in nuclear medium. This feature is kept both in 3D and 2D cases. We visualize how the strong force fields inside the nucleon in the 2D plane are distributed and illustrate how these forces undergo change in nuclear matter.

1 Introduction

The gravitational form factors (GFFs) or the energy–momentum tensor (EMT) form factors (FFs) of the nucleon provide essential information on the mass, spin, pressure, and shear-force distributions. In particular, the force distributions inside a nucleon shed light on how the nucleon acquires stability microscopically. While the GFFs were proposed many years ago [1,2], it is practically impossible to measure them directly. However, the generalized parton distributions (GPDs) furnish a modern understanding of the form factors. The electromagnetic form factors and GFFs are identified as the first and second moments of the vector GPDs [3–5] (see also relevant reviews [6–8]), respectively. It indicates that the GFFs of the nucleon can be extracted from the experimental data on the vector GPDs [9–12]. The GFFs reveal a unique feature of the mechanical structure of the nucleon: Any hadron should satisfy the stability condition, also known as the von Laue condition [13], which arises from the conservation of the EMT current (see, for example, a recent review [14]). It is a nontrivial condition and yet any approach for describing the structure of the nucleon should comply with it.

The D-term form factor of the nucleon, which is one of the GFFs, is associated with the pressure and shear-force distributions, which carry information on the mechanism of the nucleon stabilization and dictate a criterion for the stability condition of the nucleon [14–16]. These three-dimensional (3D) distributions of the pressure and shear-force are often presented in the Breit frame (BF) [14,15,17]. On the other hand, the validity of the 3D densities for the nucleon [8,18–23] has been under question since the experiments on the proton structure performed by Hofstadter [24,25]. The criticisms have it that the 3D distributions are valid only for the nonrelativistic particles such as atoms and nuclei, the intrinsic sizes of which are much larger than the characteristic Compton wavelength ($\lambda\!\!\!^{-} = \hbar/mc$). However, when it comes to the nucleon, one cannot define a localized state because the intrinsic size of the nucleon bears comparison with its Compton wavelength. It implies that the nucleon is per se

[a] e-mail: Jun-Young.Kim@ruhr-uni-bochum.de
[b] e-mail: yakhshiev@inha.ac.kr
[c] e-mail: hchkim@inha.ac.kr (corresponding author)

a relativistic particle [8], so that the probabilistic interpretation of its 3D distributions in the BF is tainted by relativistic corrections.

Nevertheless, the BF distributions for the static EMT can be interpreted as quasi-probabilistic densities from the phase-space perspective [16,26–29]. It means that the BF distributions, which are defined through the Wigner distributions in the quantum phase space [30,31], can be understood as quasi-probabilistic ones due to Heisenberg's uncertainty principle. If one takes the infinite momentum frame (IMF), which indicates that the nucleon is on the light-front (LF), the relativistic corrections to the distributions are suppressed kinematically and a transversely localized state for the nucleon can be defined, which enables one to construct the two-dimensional (2D) transverse distributions on the LF. They provide a strict probabilistic interpretation [20,21,32] and are not Lorentz contracted since the initial and final states of the nucleon lie on the mass shell. Recently, it was shown in Refs. [28,33,34] that the BF charge distributions could be interpolated to the LF ones. In Ref. [35], this interpolation was applied to the EMT force distributions as well as the electromagnetic ones [33,36,37]. The Abel transform [38], which has been used in the computerized medical tomography [39], brings the 3D BF distributions to the 2D LF ones in the transverse plane. It was already utilized in the deeply virtual Compton scattering [40,41]. As pointed out in Ref. [35], it is crucial to scrutinize how the EMT force distributions in the BF are related to those in the IMF.

In Ref. [42] the Abel transformation from the 3D BF distributions to the 2D IMF ones was criticized. That in Ref. [42] was defined by integrating a spherical symmetric 3D distribution merely over z-axis. It means that the integral projects the 3D BF distribution onto the 2D BF one without any relativistic effects. Thus, the Abel transformation defined in Ref. [42] is restricted within the BF, so that their Abel images are different from those defined in Refs. [33,35,36]. As far as the EM and EMT transverse densities of the nucleon are concerned, we can project the 3D distributions onto the 2D transverse densities in the LF. Contrary to the criticism raised in Ref. [42], the 2D IMF transverse charge densities of the nucleon [21] were successfully reproduced by Abel-transforming the nonrelativistic 3D charge and magnetization distributions in Ref. [33]. Thus, the criticism of Ref. [42] was not applied to the present definition of the Abel transform. We want to stress again that while the Abel transformation used in this literature is quite different from the typical Abel transformation, we implicitly define "Abel transformation" as the projection of the 3D BF distributions onto 2D IMF ones. We will show in the current work that the EMT transverse densities in the LF are indeed derived by the Abel transformation of the EMT distributions in the 3D BF as done in Ref. [35].

It is also of great interest to examine how the mechanical properties of the nucleon undergo modification in nuclear matter. In fact, the GFFs of the nucleon in nuclear medium were already studied in Ref. [43]. In the present work, we aim at providing the genuine 2D EMT distributions of the nucleon in nuclear matter in the IMF. To investigate them, we employ the in-medium modified Skyrme model [43–45]. The model is known to be one of the simplest ones for describing the lowest-lying baryons based on the $1/N_c$ expansion. In the large N_c limit, a baryon arises as a chiral soliton with effective mesonic degrees of freedom [46] on account of the suppression of the meson fluctuation. In addition, the model is related to the essential properties of the QCD, such as chiral symmetry and its spontaneous breaking.

Qualitatively, the model quite satisfactorily describes the important properties of the nucleon at low-energy regime. The merit of the model is that it can be easily applied to study the numerous baryon properties and has even described well the general properties of the nucleon GFFs. This model was already extended to consider the nucleon properties in nuclear matter by modifying the properties of mesons in medium [44,45]. In Ref. [47], the model has been further elaborated to consider the nuclear matter properties at saturation density where the stabilizing term was refined in nuclear medium. In the present work, we will take Ref. [47] as our model framework to revisit the GFFs and the 3D distributions of the nucleon in nuclear matter and study the modification of the 2D images of the nucleon pressure and shear-force distributions.

The present work is organized as follows: In Sect. 2, we formulate the 2D and 3D EMT distributions of the nucleon in general. In Sect. 3, we show how to compute the GFFs of the nucleon in nuclear matter. In Sect. 4, we present the results and discuss them, focusing on how the strong force fields are distributed inside a nucleon in nuclear matter. The final section summarizes the present work draws conclusions.

2 2D and 3D EMT distributions of the nucleon

We first recapitulate the GFFs of the nucleon [1,2]. The nucleon matrix element of symmetric EMT operator $\hat{T}^{\mu\nu}(0)$ between the nucleon states with initial(final) momentum $p(p')$ and helicity $\lambda(\lambda')$ can be parametrized in terms of the three form factors $A(t)$, $J(t)$, and $D(t)$ as follows

$$\langle p',\lambda'|\hat{T}^{\mu\nu}(0)|p,\lambda\rangle = \bar{N}_{\lambda'}(p')\Big[A(t)\frac{P^\mu P^\nu}{m} + J(t)\frac{iP^{\{\mu}\sigma^{\nu\}\alpha}\Delta_\alpha}{m} + \frac{D(t)}{4m}(\Delta^\mu\Delta^\nu - g^{\mu\nu}\Delta^2)\Big]N_\lambda(p), \tag{1}$$

where $N_\lambda(p)$ is the Dirac spinor which is normalized as $\bar{N}_{\lambda'}(p)N_\lambda(p) = 2m\delta_{\lambda'\lambda}$ and we introduced kinematic variables $P^\mu = (p^\mu + p'^\mu)/2$, $\Delta^\mu = p'^\mu - p^\mu$, and $\Delta^2 = t$. The parenthesis $a^{\{\mu}b^{\nu\}} = (a^\mu b^\nu + a^\nu b^\mu)/2$ stands for the symmetrization operator and m is the nucleon mass. We also use the covariant normalization $\langle p', \lambda'|p, \lambda\rangle = 2p^0(2\pi)^3\delta_{\lambda'\lambda}\delta^{(3)}(\boldsymbol{p}' - \boldsymbol{p})$ for the one-particle states. Three different form factors, $A(t)$, $J(t)$ and $D(t)$, provide information on the mass, spin, and the mechanical properties of the nucleon, respectively. The mass form factor is given as the following linear combination

$$M(t) = A(t) - \frac{t}{4m^2}(A(t) - 2J(t) + D(t)). \tag{2}$$

In the Wigner sense, the mass $\varepsilon(r)$, angular momentum $\rho_J(r)$, pressure $p(r)$ and shear-force $s(r)$ distributions in the BF are obtained as

$$\begin{aligned}
\varepsilon(r) &= m\tilde{M}(r),\\
\rho_J(r) &= -\frac{1}{3}r\frac{d}{dr}\tilde{J}(r),\\
s(r) &= -\frac{1}{4m}r\frac{d}{dr}\frac{1}{r}\frac{d}{dr}\tilde{D}(r),\\
p(r) &= \frac{1}{6m}\frac{1}{r^2}\frac{d}{dr}r^2\frac{d}{dr}\tilde{D}(r),
\end{aligned} \tag{3}$$

by using the generic 3D inverse Fourier transform

$$\tilde{F}(r) = \int \frac{d^3\boldsymbol{\Delta}}{(2\pi)^3}e^{-i\boldsymbol{\Delta}\cdot\boldsymbol{r}}F(-\boldsymbol{\Delta}^2), \tag{4}$$

of the GFFs, where $F = A, M, J, D$ are defined in terms of the multipole expansion [14,16,48,49].

However, the physical meaning of 3D distributions is marred by ambiguity because of the relativistic corrections. This ambiguity can be remedied by considering the 2D transverse distributions in the IMF [8,19–23]. The EMT distributions in the IMF have been already extensively studied in numerous Refs. [16,26,35,50–53]. The corresponding EMT 2D distributions for the momentum $\varepsilon^{(2D)}(x_\perp)$, angular momentum $\rho_J^{(2D)}(x_\perp)$, pressure $p^{(2D)}(x_\perp)$ and shear force $s^{(2D)}(x_\perp)$, which have the following forms

$$\begin{aligned}
\varepsilon^{(2D)}(x_\perp) &= P^+\tilde{A}(x_\perp),\\
\rho_J^{(2D)}(x_\perp) &= -\frac{1}{2}x_\perp\frac{d}{dx_\perp}\tilde{J}(x_\perp),\\
s^{(2D)}(x_\perp) &= -\frac{1}{4P^+}x_\perp\frac{1}{dx_\perp}\frac{1}{x_\perp}\frac{d}{dx_\perp}\tilde{D}(x_\perp),\\
p^{(2D)}(x_\perp) &= \frac{1}{8P^+}\frac{1}{x_\perp}\frac{d}{dx_\perp}x_\perp\frac{d}{dx_\perp}\tilde{D}(x_\perp),
\end{aligned} \tag{5}$$

were obtained by using the generic 2D inverse Fourier transform

$$\tilde{F}(x_\perp) = \int \frac{d^2\boldsymbol{\Delta}_\perp}{(2\pi)^2}e^{-i\boldsymbol{\Delta}_\perp\cdot\boldsymbol{x}_\perp}F(-\boldsymbol{\Delta}_\perp^2). \tag{6}$$

of the corresponding GFFs. In the expressions above $\boldsymbol{x}_\perp$ and $\boldsymbol{\Delta}_\perp$ denote the position and momentum vectors in the 2D plane transverse to the moving direction of the nucleon, respectively. Consequently, the mass, shear force, and pressure distributions are redefined by multiplying, for convenience, the Lorentz factors [35] as follows

$$\begin{aligned}
\mathcal{E}(x_\perp) &= \frac{m}{P^+}\varepsilon^{(2D)}(x_\perp),\\
\mathcal{S}(x_\perp) &= \frac{P^+}{2m}s^{(2D)}(x_\perp),\\
\mathcal{P}(x_\perp) &= \frac{P^+}{2m}p^{(2D)}(x_\perp),
\end{aligned} \tag{7}$$

where P^+ is the light-cone momentum. Since the light-cone momentum distribution $\varepsilon^{(2D)}(x_\perp)$ is rescaled by the factor m/P^+, we will name $\mathcal{E}(x_\perp)$ as the "*2D IMF energy distribution*". One should keep in mind that it does not indicate the higher-twist distribution normalized to be P^-.

The BF and LF distributions given respectively in Eqs. (3) and (7) should be related to each other and the corresponding relations were derived in Refs. [35,36] by the Abel transform

$$\begin{aligned}
\left(1 - \frac{\partial^2_{(2D)}}{4m^2}\right)\mathcal{E}(x_\perp) &= 2\int_{x_\perp}^\infty \frac{rdr}{\sqrt{r^2 - x_\perp^2}}\Big[\varepsilon(r)\\
&\quad + \frac{3}{2}p(r) + \frac{3}{2mr^2}\frac{d}{dr}r\rho_J(r)\Big],\\
\rho_J^{(2D)}(x_\perp) &= 3\int_{x_\perp}^\infty \frac{\rho_J(r)}{r}\frac{x_\perp^2 dr}{\sqrt{r^2 - x_\perp^2}},\\
\mathcal{S}(x_\perp) &= \int_{x_\perp}^\infty \frac{s(r)}{r}\frac{x_\perp^2 dr}{\sqrt{r^2 - x_\perp^2}},\\
\frac{1}{2}\mathcal{S}(x_\perp) + \mathcal{P}(x_\perp) &= \frac{1}{2}\int_{x_\perp}^\infty \left(\frac{2}{3}s(r) + p(r)\right)\\
&\quad \times \frac{rdr}{\sqrt{r^2 - x_\perp^2}}.
\end{aligned} \tag{8}$$

In the large N_c limit, it is possible to derive the reduced expression for the 2D energy distribution

$$\mathcal{E}(x_\perp) = 2\int_{x_\perp}^\infty \frac{rdr}{\sqrt{r^2 - x_\perp^2}}\left[\varepsilon(r) + \frac{3}{2}p(r)\right]. \tag{9}$$

Integrating 2D and 3D EMT distributions over $\boldsymbol{x}_\perp$ and $\boldsymbol{r}$, respectively, one can get the mass and spin of the nucleon

$$\begin{aligned} mA(0) &= \int d^2x_\perp\, \mathcal{E}(x_\perp) = \int d^3r\, \varepsilon(r), \\ J(0) &= \int d^2x_\perp\, \rho_J^{(2D)}(x_\perp) = \int d^3r\, \rho_J(r), \end{aligned} \tag{10}$$

with the properly normalized form factors, $A(0) = 1$ and $J(0) = 1/2$. As in the case of the radii for the 3D distributions [54], we can define 2D radii for the mass and angular momentum

$$\begin{aligned} \langle x_\perp^2\rangle_{\mathcal{E}} &= \frac{1}{m}\int d^2x_\perp x_\perp^2 \mathcal{E}(x_\perp) \\ &= \frac{2}{3}\langle r^2\rangle_\varepsilon + \frac{D(0)}{m^2}, \\ \langle x_\perp^2\rangle_J &= 2\int d^2x_\perp x_\perp^2 \rho_J^{(2D)}(x_\perp) = \frac{4}{5}\langle r^2\rangle_J, \end{aligned} \tag{11}$$

respectively [35].

The conservation of the EMT current also provides the 2D stability condition for the nucleon as in the 3D case, which yields the following 2D stability equation

$$\mathcal{P}'(x_\perp) + \frac{\mathcal{S}(x_\perp)}{x_\perp} + \frac{1}{2}\mathcal{S}'(x_\perp) = 0. \tag{12}$$

This 2D stability condition can be considered to be equivalent to the 3D expression

$$p'(r) + \frac{2s(r)}{r} + \frac{2}{3}s'(r) = 0. \tag{13}$$

One can see that the shear-force and pressure distributions are related to each other. Using Eqs. (12) and (13), we obtain the global stability condition or the von Laue condition

$$\int d^3r\, p(r) = 0 \iff \int d^2x_\perp \mathcal{P}(x_\perp) = 0, \tag{14}$$

$$\int_0^\infty dr\, r\left[p(r) - \frac{1}{3}s(r)\right] = 0 \iff \int_0^\infty dx_\perp \left[\mathcal{P}(x_\perp) - \frac{1}{2}\mathcal{S}(x_\perp)\right] = 0, \tag{15}$$

which is the necessary condition for the stability of the nucleon. The integrand in the last equation in Eq. (8) gives the 3D local stability condition, which leads to the 2D local stability condition in the LF [35]

$$\frac{2}{3}s(r) + p(r) > 0 \iff \frac{1}{2}\mathcal{S}(x_\perp) + \mathcal{P}(x_\perp) > 0. \tag{16}$$

The positivity is kept intact by the Abel transformation. This implies that though the 3D distributions have only quasi-probabilistic meaning, they still provide intuitive features for the stability conditions. It also relates the 3D mechanical radius to the 2D one

$$\begin{aligned} \langle x_\perp^2\rangle_{\text{mech}} &= \frac{\int d^2x_\perp x_\perp^2 \left(\frac{1}{2}\mathcal{S}(x_\perp) + \mathcal{P}(x_\perp)\right)}{\int d^2x_\perp \left(\frac{1}{2}\mathcal{S}(x_\perp) + \mathcal{P}(x_\perp)\right)} \\ &= \frac{4D(0)}{\int_{-\infty}^0 dt\, D(t)} = \frac{2}{3}\langle r^2\rangle_{\text{mech}}. \end{aligned} \tag{17}$$

To understand the physics of the pressure and shear-force distributions more in detail, it is instructive to introduce the notion of the normal and tangential force fields that are just the eigenvalues of the stress tensor contracted with the radial $\boldsymbol{e}_r$ and tangential $\boldsymbol{e}_\phi$ unit vectors, respectively. The 3D and the 2D force fields in the BF and LF are expressed in terms of the pressure and shear-force distributions as follows:

$$\begin{aligned} F_n(r) &= 4\pi r^2\left[\frac{2}{3}s(r) + p(r)\right], \\ F_t(r) &= 4\pi r^2\left[-\frac{1}{3}s(r) + p(r)\right], \\ F_n^{(2D)}(x_\perp) &= 2\pi x_\perp\left[\frac{1}{2}\mathcal{S}(x_\perp) + \mathcal{P}(x_\perp)\right], \\ F_t^{(2D)}(x_\perp) &= 2\pi x_\perp\left[-\frac{1}{2}\mathcal{S}(x_\perp) + \mathcal{P}(x_\perp)\right]. \end{aligned} \tag{18}$$

Equation (18) implies that $F_n(r)$ and $F_n^{(2D)}(x_\perp)$ should be positive because of the local stability condition in Eq. (16), whereas $F_t(r)$ and $F_t^{(2D)}(x_\perp)$ should have at least one nodal point to ensure the von Laue conditions, which are shown in Eq. (15). We will see these characteristics of the force fields later in detail.

The value of the D-term is determined by integrating over the 3D and 2D pressure or shear-force distributions as

$$\begin{aligned} D(0) &= -\frac{4m}{15}\int d^3r\, r^2 s(r) = -m\int d^2x_\perp x_\perp^2 \mathcal{S}(x_\perp) \\ &= m\int d^3r\, r^2 p(r) = 4m\int d^2x_\perp x_\perp^2 \mathcal{P}(x_\perp). \end{aligned} \tag{19}$$

As will be shown soon, both the 2D and 3D shear-force distributions are positive in the overall ranges of $x_\perp$ and r, respectively. So, the $D(0)$ should be always negative, which is also deeply related to the stability conditions. Equation (19) also shows the equivalence between the 2D and 3D pressure and shear-force distributions. It implies that while 3D distributions are quasi-probabilistic, the 2D distributions provide the proper probabilistic meaning.

3 Gravitational form factors of the nucleon in nuclear matter

To compute the GFFs of the nucleon in nuclear matter, we will employ the in-medium modified chiral soliton model. We start with the in-medium modified chiral Lagrangian[1] [43,47]

$$\begin{aligned}\mathcal{L}^* &= \mathcal{L}_2^* + \mathcal{L}_4^* + \mathcal{L}_{\rm m}^* \\ &= \frac{F_\pi^2}{16}{\rm Tr}\left[\partial_0 U \partial^0 U^\dagger\right] + \alpha_p \frac{F_\pi^2}{16}{\rm Tr}\left[\partial_i U \partial^i U^\dagger\right] \\ &\quad + \frac{1}{32e^2\gamma}{\rm Tr}\left[(\partial_\mu U)U^\dagger, (\partial_\nu U)U^\dagger\right]^2 \\ &\quad + \alpha_s \frac{m_\pi^2 F_\pi^2}{8}{\rm Tr}\left[U-1\right], \end{aligned} \tag{20}$$

where $U = \exp[\hat{r}^i \tau^i P(r)]$ is the SU(2) chiral field with the profile function $P(r)$ for the pion fields, τ^i $(i = 1, 2, 3)$ are the Pauli matrices, and $\hat{r}^i = r^i/|\boldsymbol{r}|$ is the radial component of the unit vector in space. Tr stands for the trace running over the SU(2) isospin space. The input parameters of the soliton model are given by the pion decay constant $F_\pi = 108.78\,{\rm MeV}$, a dimensionless parameter $e = 4.854$, and the pion mass $m_\pi = 135\,{\rm MeV}$.

We incorporate the medium modifications by introducing the density-dependent medium functions

$$\begin{aligned}&\alpha_p(\rho) = 1 - \chi_p(\rho), \quad \chi_p(\rho) = \frac{4\pi c_0 \rho}{\eta + 4\pi c_0 g' \rho}, \\ &\eta = 1 + \frac{m_\pi}{m}, \\ &\alpha_s(\rho) = 1 + \frac{\chi_s(\rho)}{m_\pi^2}, \quad \chi_s(\rho) = -4\pi\eta b_0 \rho, \\ &\gamma(\rho) = \exp\left[-\frac{\gamma_{\rm num}\rho}{1+\gamma_{\rm den}\rho}\right], \end{aligned} \tag{21}$$

which associate the model with the low energy pion-nucleus scattering data and properties of nuclear matter at the normal nuclear matter density or the saturation point ρ_0 [47]. The parameters in the medium functions have been already fixed by

$$\begin{aligned} &b_0 = -0.024\, m_\pi^{-1}, \quad c_0 = 0.09\, m_\pi^{-3}, \quad g' = 0.7, \\ &\gamma_{\rm num} = 0.797\, m_\pi^{-3}, \quad \gamma_{\rm den} = 0.496\, m_\pi^{-3}, \end{aligned} \tag{22}$$

where b_0 and c_0 are s- and p-wave pion-nucleon scattering lengths and volumes, g' is correlation parameter, and $\gamma_{\rm num}$ and $\gamma_{\rm den}$ are fitted in such a way that nuclear matter properties at the normal nuclear matter density $\rho_0 = 0.5 m_\pi^3$ are reproduced correctly. For details we refer to Ref. [47].

Since we consider homogeneous nuclear matter, where the nuclear density is kept constant, we treat the modified chiral Lagrangian by introducing the renormalized effective constants:

$$\begin{aligned} &F_{\pi,t}^* = F_{\pi,t} = F_\pi, \quad F_{\pi,s}^* = \alpha_p^{1/2} F_\pi, \\ &e^* = \gamma^{1/2} e, \quad m_\pi^* = (\alpha_s/\alpha_p)^{1/2} m_\pi, \end{aligned} \tag{23}$$

which shows that all expressions can be expressed in terms of the renormalized model parameters. For example, the classical soliton mass functional in nuclear matter takes the following form

$$\begin{aligned} M_{\rm sol}^*[P] = 4\pi \int_0^\infty dr\, r^2 &\times \left[\frac{F_{\pi,s}^{*2}}{8}\left(\frac{2\sin^2 P(r)}{r^2} + P'(r)^2\right)\right. \\ &+ \frac{\sin^2 P(r)}{2e^{*2}r^2}\left(\frac{\sin^2 P(r)}{r^2} + 2P'(r)^2\right) \\ &\left. + \frac{m_\pi^{*2} F_{\pi,s}^{*2}}{4}\left(1 - \cos P(r)\right)\right], \end{aligned} \tag{24}$$

where $P'(r)$ denotes the derivative with respect to the variable r. Minimizing the soliton mass, we obtain the nonlinear differential equation for the profile function $P(r)$ and the solution for the baryon number $B = 1$ is derived by imposing the boundary conditions, $P(0) = \pi$ and $P(\infty) = 0$. Then making a zero-mode quantization or rotating the classical soliton slowly, we get the time-dependent SU(2) soliton $U(\boldsymbol{r}) \to A(t)U(\boldsymbol{r})A^\dagger(t)$ with the collective Hamiltonian [46]

$$H^* = M_{\rm sol}^* + \frac{\hat{\boldsymbol{J}}^2}{2I^*}, \tag{25}$$

where $\hat{\boldsymbol{J}}$ is angular momentum operator and

$$\begin{aligned} I^* = \frac{2\pi}{3}\int_0^\infty dr\, r^2 \sin^2 P(r) \\ \times \left[F_\pi^2 + \frac{4P'(r)^2}{e^{*2}} + \frac{4\sin^2 P(r)}{e^{*2}r^2}\right] \end{aligned} \tag{26}$$

is the moment of inertia of the rotating soliton. We derive the EMT from the time-dependent Lagrangian for the rotating soliton

$$T^{\mu\nu *} = \frac{\partial \mathcal{L}^*}{\partial(\partial_\mu \phi_a)}\partial^\nu \phi_a - g^{\mu\nu}\mathcal{L}^*, \tag{27}$$

[1] Hereafter, a superscript "*" indicates an modified in-medium quantity. We consider the in-medium modifications of the quantities discussed so far with the superscript included.

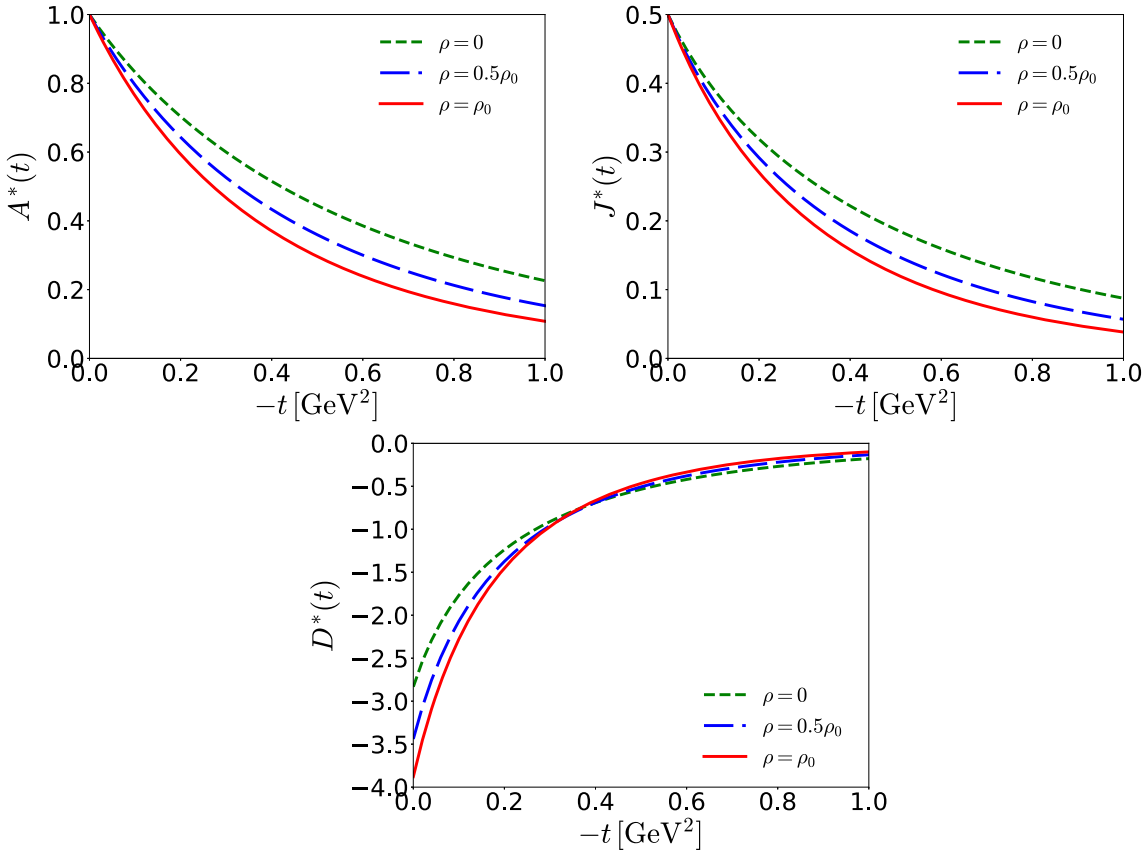

Fig. 1 The GFFs $A^*(t)$, $J^*(t)$, and $D^*(t)$ of the nucleon as functions of the momentum transfer t. The short-dashed curves draw those in free space, whereas the long-dashed and solid ones depict those respectively at $\rho = 0.5\rho_0$ and at $\rho = \rho_0$, where $\rho_0 = 0.5\, m_\pi^3$ is the normal nuclear matter density

where ϕ_a is a time-dependent pionic field with $U(t,r) = \phi_0 + i\boldsymbol{\tau}\cdot\boldsymbol{\phi}$ that satisfied the unitarity condition $\phi_0^2 + \boldsymbol{\phi}^2 = 1$. As discussed already in Ref. [55,56], one should carefully take the following procedure to describe the EMT form factors consistently within the Skyrme model. We first minimize the classical soliton mass, and then make a collective quantization. This means that any observable can be decomposed into two different contributions:

$$A = A_{\mathrm{LO}} + A_{\mathrm{rot}}, \tag{28}$$

where A_{LO} denotes the leading-order contribution in the $1/N_c$ expansion whereas A_{rot} comes from the $1/N_c$ rotational corrections. One should keep in mind that time dependence of the collective Lagrangian enters implicitly through the collective quantization, not explicitly. When A_{LO} does not vanish, we shall suppress the rotational corrections A_{rot}. In the $1/N_c$ expansion, this procedure is a rigorous one. A detailed discussion can be found in Appendix C of Ref. [56]. Thus, as far as we follow this procedure, the EMT current is conserved.

The components of the EMT are then written as

$$\begin{aligned}
T^{00*} &= \delta_{\sigma'\sigma}\left[\frac{F_{\pi,s}^{*2}}{8}\left(\frac{2\sin^2 P(r)}{r^2} + P'(r)^2\right)\right.\\
&\quad + \frac{\sin^2 P(r)}{2e^{*2}r^2}\left(\frac{\sin^2 P(r)}{r^2} + 2P'(r)^2\right)\\
&\quad \left. + \frac{m_\pi^{*2}F_{\pi,s}^{*2}}{4}\left(1-\cos P(r)\right)\right],\\
T^{ij*} &= \hat{r}^i\hat{r}^j\delta_{\sigma'\sigma}\left[\left(\frac{F_{\pi,s}^{*2}}{4} + \frac{\sin^2 P(r)}{e^{*2}r^2}\right)\right.\\
&\quad \left.\times\left(P'(r)^2 - \frac{\sin^2 P(r)}{r^2}\right)\right]\\
&\quad + \delta^{ij}\delta_{\sigma'\sigma}\left[-\frac{F_{\pi,s}^{*2}}{8}P'(r)^2 + \frac{\sin^4 P(r)}{2e^{*2}r^4}\right.\\
&\quad \left. - \frac{m_\pi^{*2}F_{\pi,s}^{*2}}{4}\left(1-\cos P(r)\right)\right],\\
T^{0k*} &= (\hat{\boldsymbol{J}}\times\hat{\boldsymbol{r}})^k_{\sigma'\sigma}\frac{\sin^2 P(r)}{4I^*r}
\end{aligned}$$

$$\times \left[F_\pi^2 + \frac{4\sin^2 P(r)}{e^{*2}r^2} + \frac{4P'(r)^2}{e^{*2}} \right]. \tag{29}$$

The time component T^{00*} yields the leading-order term for the energy, i.e., for the static mass distribution given by the integrand in Eq. (24). The mixed space-time components T^{0k*} give the angular momentum density whereas the spatial ones T^{ij*} furnish the pressure and shear-force densities.

We can extract the energy, spin, pressure, and shear-force distributions directly from Eq. (29):

$$\begin{aligned}
\varepsilon^*(r) &= \left[\frac{F_{\pi,s}^{*2}}{8} \left(\frac{2\sin^2 P(r)}{r^2} + P'(r)^2 \right) \right. \\
&\quad + \frac{\sin^2 P(r)}{2e^{*2}r^2} \left(\frac{\sin^2 P(r)}{r^2} + 2P'(r)^2 \right) \\
&\quad \left. + \frac{m_\pi^{*2} F_{\pi,s}^{*2}}{4} (1 - \cos P(r)) \right], \\
\rho_J^*(r) &= \frac{\sin^2 P(r)}{12I^*} \left[F_\pi^2 + \frac{4\sin^2 P(r)}{e^{*2}r^2} + \frac{4P'(r)^2}{e^{*2}} \right], \\
p^*(r) &= -\frac{F_{\pi,s}^{*2}}{24} \left(\frac{2\sin^2 P(r)}{r^2} + P'(r)^2 \right) \\
&\quad + \frac{\sin^2 P(r)}{6e^{*2}r^2} \left(\frac{\sin^2 P(r)}{r^2} + 2P'(r)^2 \right) \\
&\quad - \frac{m_\pi^{*2} F_{\pi,s}^{*2}}{4} (1 - \cos P(r)), \\
s^*(r) &= \left(\frac{F_{\pi,s}^{*2}}{4} + \frac{\sin^2 P(r)}{e^{*2}r^2} \right) \\
&\quad \times \left(P'(r)^2 - \frac{\sin^2 P(r)}{r^2} \right).
\end{aligned} \tag{30}$$

As mentioned previously, the rotational corrections are suppressed except for the spin density $\rho_J(r)$, where the rotational corrections take the leading role.

We then arrive at the final expressions for the GFFs in Eq. (1) given in the large N_c limit as

$$A^*(t) - \frac{t}{4m^{*2}} D^*(t) = \frac{1}{m^*} \int \mathrm{d}^3\boldsymbol{r} \times \varepsilon^*(r)\ j_0(r\sqrt{-t}), \tag{31}$$

$$D^*(t) = 6m^* \int \mathrm{d}^3\boldsymbol{r}\ p^*(r)\ \frac{j_0(r\sqrt{-t})}{t}, \tag{32}$$

$$J^*(t) = 3 \int \mathrm{d}^3\boldsymbol{r}\ \rho_J^*(r)\ \frac{j_1(r\sqrt{-t})}{r\sqrt{-t}}, \tag{33}$$

where $j_0(z)$ and $j_1(z)$ represent the spherical Bessel functions of order 0 and 1, respectively. At the zero momentum transfer $t = 0$, $A^*(0)$ and $J^*(0)$ are normalized to be

Table 1 Various quantities related to the GFFs of the nucleon in both the BF and IMF: the energy distributions at the center ($\varepsilon^*(0)$, $\mathcal{E}^*(0)$), the pressure distributions at the center ($p^*(0)$, $\mathcal{P}^*(0)$), nodal points of the pressures (r_0^*, $(x_\perp^*)_0$)) and the mean square radii of the mass, angular momentum and mechanical ($\langle r^2\rangle^*$, $\langle x_\perp^2\rangle^*$) at different values of nuclear density ρ

ρ/ρ_0	0	0.5	1
$\varepsilon^*(0)$ (GeV/fm^3)	1.25	0.84	0.62
$p^*(0)$ (GeV/fm^3)	0.263	0.178	0.133
r_0^* (fm)	0.72	0.82	0.91
$\langle r^2\rangle_\varepsilon^*$ (fm^2)	0.68	0.83	0.95
$\langle r^2\rangle_J^*$ (fm^2)	1.09	1.23	1.35
$\langle r^2\rangle_{\mathrm{mech}}^*$ (fm^2)	0.75	0.90	1.01
$\mathcal{E}^*(0)$ (GeV/fm^2)	1.25	0.96	0.80
$\mathcal{P}^*(0)$ (GeV/fm^2)	0.060	0.047	0.039
$(x_\perp)_0^*$ (fm)	0.59	0.67	0.73
$\langle x_\perp^2\rangle_\mathcal{E}^*$ (fm^2)	0.30	0.38	0.44
$\langle x_\perp^2\rangle_J^*$ (fm^2)	0.87	0.99	1.08
$\langle x_\perp^2\rangle_{\mathrm{mech}}^*$ (fm^2)	0.50	0.60	0.68

$$A^*(0) = \frac{1}{m^*} \int \mathrm{d}^3\boldsymbol{r}\ \varepsilon^*(r) = 1,$$
$$J^*(0) = \int \mathrm{d}^3\boldsymbol{r}\ \rho_J^*(r) = \frac{1}{2}. \tag{34}$$

These normalizations were proven in Ref. [56] for a Skyrmion in free space and they hold also in nuclear matter [43].

4 Results and discussion

To examine how the mechanical properties of the nucleon undergo modification in nuclear matter, we consider homogeneous nuclear matter in which the nuclear density is kept constant. From now on, all observables are given as functions of the normalized nuclear matter density ρ/ρ_0.

4.1 Gravitational form factors of the nucleon

The GFFs of the nucleon and the corresponding 3D densities in nuclear matter were already studied in Ref. [43]. Since, however, the 3D distributions acquire ambiguous relativistic corrections because of the relativistic nature of the nucleon, they do not give a correct probabilistic meaning. Thus, we need to consider the 2D distributions of the nucleon in the LF, which provide proper probabilistic meaning. We can obtain the 2D densities in the LF by using the Abel transformation.

In Fig. 1, we show the results of the nucleon GFFs as functions of t, changing the nuclear densities from $\rho = 0$ (free space) to $\rho = \rho_0$. As ρ increases, The form factors fall off faster than those in free space as functions of t. Since

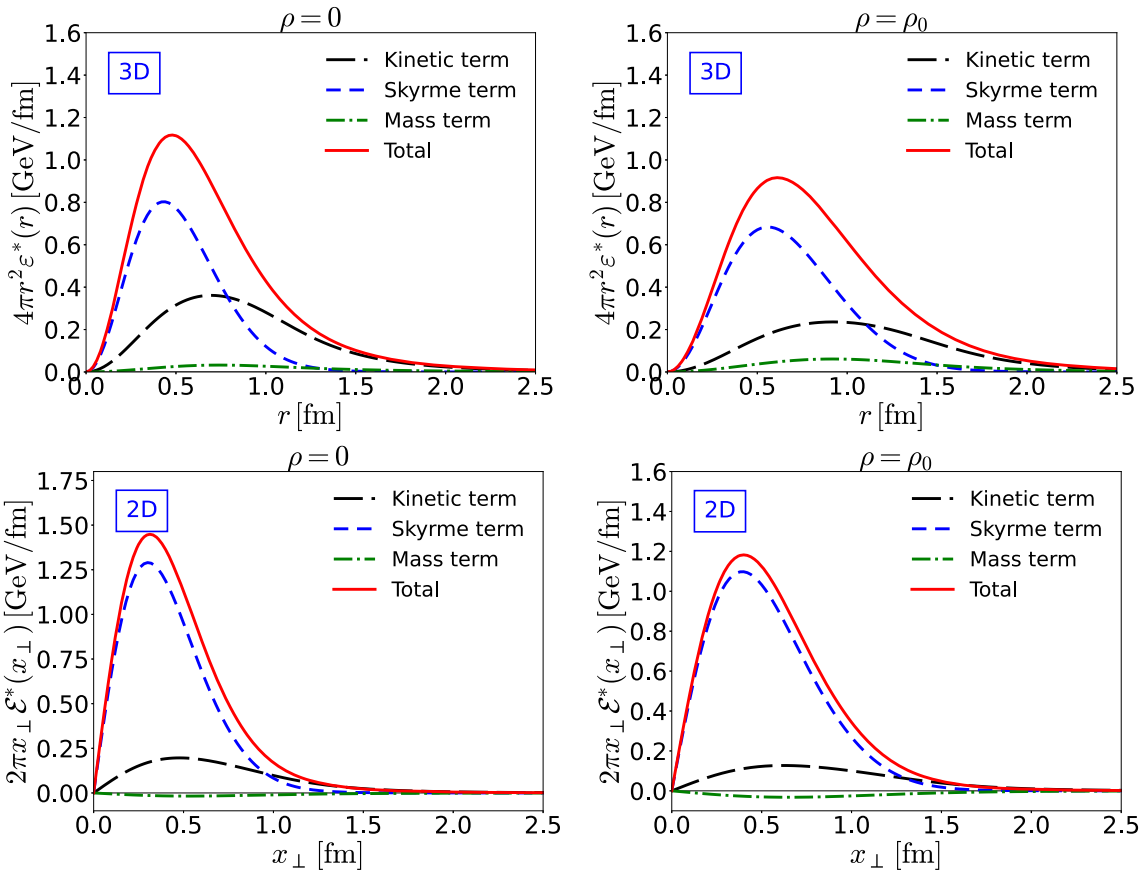

Fig. 2 The 3D and 2D mass distributions multiplied respectively by $4\pi r^2$ and $2\pi x_\perp$. The upper-left (-right) panel depicts 3D mass distributions with $4\pi r^2$ at $\rho = 0$ ($\rho = \rho_0$). The long-dashed, short-dashed, dot-dashed, and solid curves illustrate the contributions of the kinetic term ($\mathcal{L}_2^*$) with two derivatives, the Skyrme term ($\mathcal{L}_4^*$) with four derivatives, the mass term ($\mathcal{L}_m^*$), and the total result, respectively. The lower-left (-right) panel draws the 2D mass distributions with $2\pi x_\perp$ at $\rho = 0$ ($\rho = \rho_0$). Notations are the same as in the 3D case

$A^*(0) = 1$ and $J^*(0) = 1/2$ are strictly constrained to be at $t = 0$, their magnitudes are unchanged in nuclear matter. It hints that the corresponding radii of the nucleon get larger in the medium, i.e., the size of the nucleon swells in medium, as was discussed in Ref. [43]. On the other hand, the absolute magnitude of the in-medium $D^*(t)$ is enhanced by the density effects but decreases more noticeably than that in free space as t increases. The D-term form factor contains information on the stability of the nucleon and characterizes the distribution of force fields inside the nucleon. Many theoretical studies and experimental indications show that it should be negative [9,17,57–60] to secure the stability of the nucleon. In the present work, $D(0)$ is around -2.8 in free space, but it decreases (becomes larger in the absolute value) as ρ increases. $D^*(0)$ at the normal nuclear matter density yields around -3.9. This result indicates that the pressure and shear-force densities are deformed inside the nucleon by the nuclear environment. In this context, it is interesting to note that the analysis of selected nuclear isotopes with spin-parity quantum numbers $J^P = 0^+$ shows the increasing absolute value of $D(0)$ [61]. For heavier nuclei, the value of the D-term predicted in the framework of the liquid drop model is approximated as $D(0) \approx -0.246A^{2.26}$, where A is the mass number of the nucleus [15]. For more discussion, we also refer to Ref. [14].

4.2 Energy and angular momentum distributions of the nucleon

We now discuss the results for the energy distributions of the nucleon in nuclear matter. In Table 1, various quantities related to the GFFs of the nucleon are presented both in free space and in nuclear matter at the different values of nuclear density ρ. The 3D $\varepsilon^*(0)$ and 2D $\mathcal{E}^*(0)$ at the center of the nucleon decrease if ρ increases. Moreover, as listed in Table 1, the central value of the 3D distribution lessens faster than that of the 2D case. For example, the central value of the 3D distribution decreases by about 50 %, whereas it decreases by about 36 % in the 2D case.

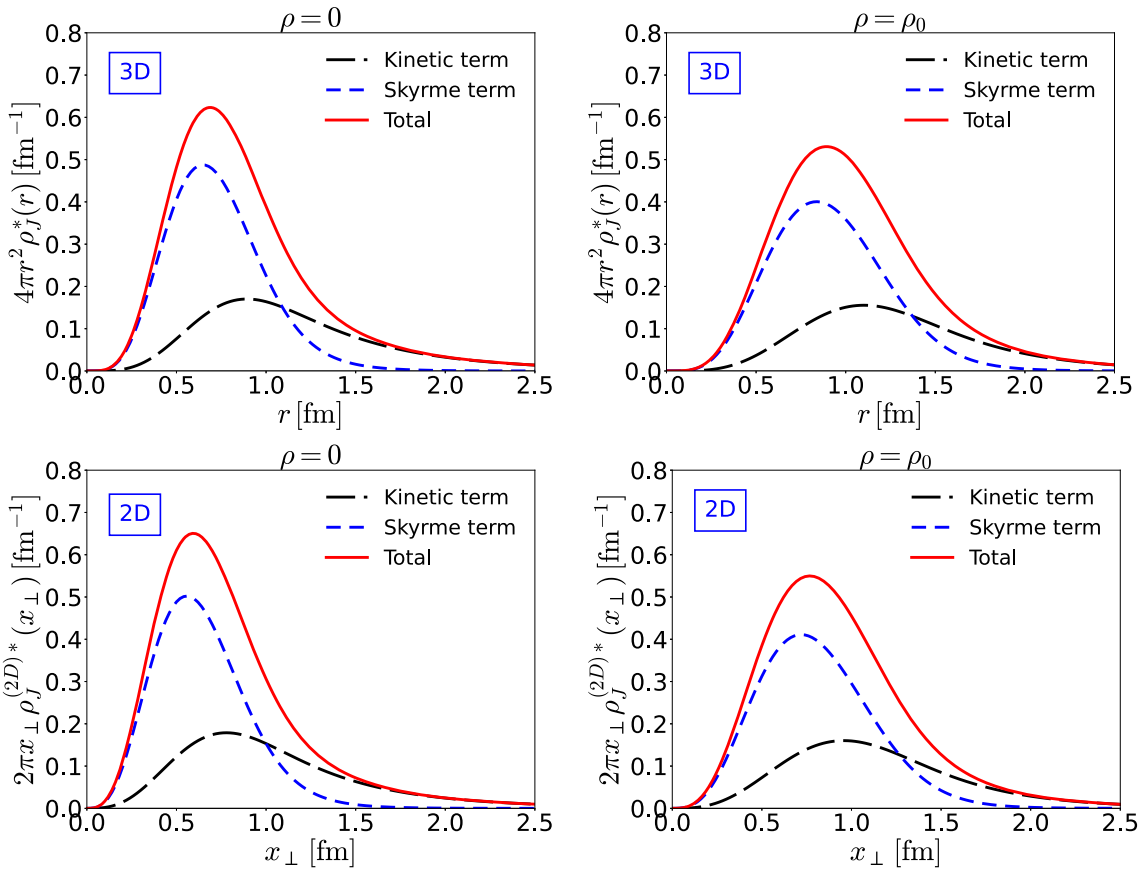

Fig. 3 The 3D angular momentum distributions of the nucleon. The upper-left (-right) panel depicts the 3D angular momentum distributions multiplied by $4\pi r^2$ at $\rho = 0$ ($\rho = \rho_0$). The lower-left (-right) panel draws the 2D angular momentum distributions with $2\pi x_\perp$ at $\rho = 0$ ($\rho = \rho_0$). Notations are the same as in Fig. 2

Table 2 Contributions of the different terms to the angular momentum J, the stability condition (Von Laue condition), and the values of the D-term extracted from the pressure distributions for $\rho = 0$ ($\rho = \rho_0$)

Terms	J	Von Laue	D-term
3D			
$\mathcal{L}_2^*$	0.188 (0.179)	−9.55 (−7.74)	−2.78 (−3.26)
$\mathcal{L}_4^*$	0.312 (0.321)	12.45 (13.65)	1.16 (2.12)
$\mathcal{L}_\mathrm{m}^*$	–	−2.90 (−5.91)	−1.22 (−2.74)
2D			
$\mathcal{L}_2^*$	0.188 (0.179)	−4.78 (−3.87)	−2.66 (−3.21)
$\mathcal{L}_4^*$	0.312 (0.321)	6.22 (6.83)	0.64 (1.15)
$\mathcal{L}_\mathrm{m}^*$	–	−1.44 (−2.96)	−0.82 (−1.82)
Total	0.5	0	−2.83 (−3.88)

In Fig. 2, we draw the 3D and 2D mass distributions multiplied respectively by $4\pi r^2$ and $2\pi x_\perp$. We find that the 3D one exhibits a broader shape than the 2D one by comparing the solid red curve in the upper panel with the lower panel. The 2D and 3D mass distributions become broader as the density of nuclear matter increases, as seen from the solid red curve in the left panel compared to the right panel. These features appear clearly in the mean square radii of the 2D and 3D mass distributions:

$$\frac{\langle x_\perp^2 \rangle_\mathcal{E}^*}{\langle r^2 \rangle_\varepsilon^*} \approx \{0.441, 0.457, 0.463\}, \tag{35}$$

where we list the ratios of mean square radii of the 2D and 3D energy distributions given at three different values of the nuclear matter density $\rho = \{0, 0.5\rho_0, \rho_0\}$, respectively. In Eq. (11), the 2D mass radius is expressed as $\langle x_\perp^2 \rangle_\mathcal{E}^* = \frac{2}{3}\langle r^2 \rangle_\varepsilon^* + D^*(0)/m^{*2}$. The factor 2/3 comes from the geometrical difference. In addition, $D(0)$ should be negative to ensure the stability of the nucleon. Thus, it is natural for $\langle x_\perp^2 \rangle_\mathcal{E}$ to be smaller than $\langle r^2 \rangle_\varepsilon$. We list the numerical values of the 3D and 2D radii explicitly in Table 1. As a result, the 3D mass mean square radius decreases by about 40 % at the normal nuclear matter density, while in the 2D case, it is reduced by about 47 %, compared to those in free space, respectively. On the other hand, the central value of the 2D

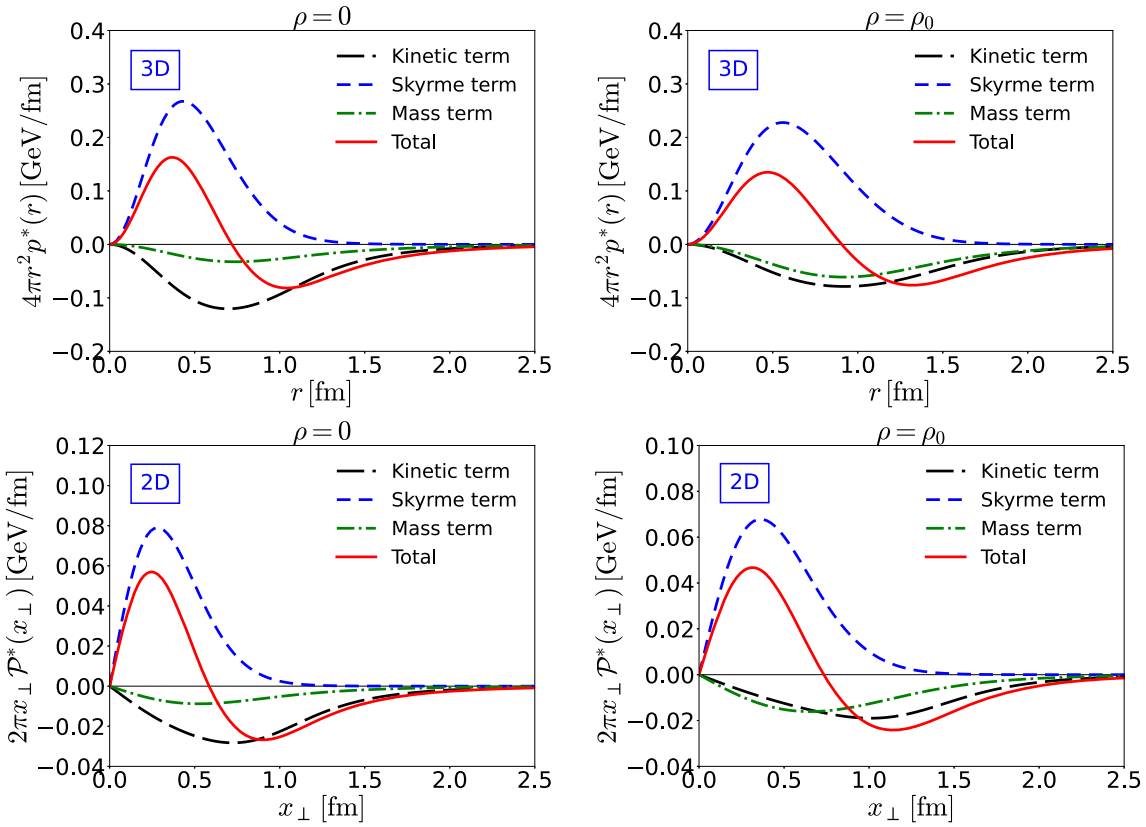

Fig. 4 3D and 2D pressure distributions of the nucleon. The upper-left (right) panel depicts the 3D pressure distributions multiplied by $4\pi r^2$ at $\rho = 0$ ($\rho = \rho_0$). The lower-left (-right) panel draws the 2D pressure distributions with $2\pi x_\perp$ at $\rho = 0$ ($\rho = \rho_0$). Notations are the same as in Fig. 2

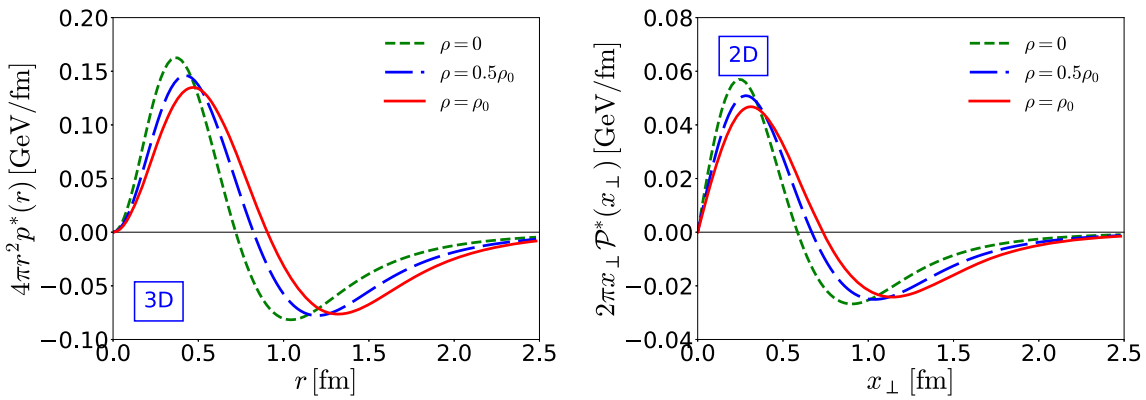

Fig. 5 3D and 2D pressure distributions of the nucleon as functions of the nuclear density ρ, multiplied by $4\pi r^2$ and $2\pi x_\perp$, respectively. The short-dashed, long-dashed, and solid curves represent the pressure distributions with $\rho = 0,\ 0.5\rho_0,\ \rho_0$, respectively. ρ_0 denotes the normal nuclear matter density

mass distribution gets larger than the 3D one as the nuclear density increases.

It is interesting to analyze how the different terms of the effective chiral Lagrangian contribute to the mass distribution. As shown in Fig. 2, all contributions become broader as the nuclear density increases. It indicates that both the internal core of the nucleon and outer shell are affected in the presence of the nuclear environment. The main contribution to the mass comes from the Skyrme term $\mathcal{L}_4^*$, whereas that of the mass term $\mathcal{L}_m^*$ turns out to be the smallest. It is of particular interest to examine how each term contributes after the Abel transformation. While the contributions from the kinetic $\mathcal{L}_2^*$ and Skyrme $\mathcal{L}_4^*$ terms preserve their sign, the mass distribution from the mass term $\mathcal{L}_m^*$ becomes negative in both the free space and nuclear matter after the Abel transformation. This behavior can be understood from Eq. (8). As

will be discussed later, mass term contributes to the pressure distribution negatively, i.e., it gives $3p(r)/2 < 0$, of which the magnitude is larger than $\varepsilon(r)$.

In Fig. 3, we depict the 3D and 2D distributions for the angular momentum, multiplied by $4\pi r^2$ and $2\pi x_\perp$, respectively. Note that integrating over the 2D and 3D angular-momentum distributions should yield the spin of the nucleon

$$\int d^2x_\perp \rho_J^{(2D)*}(x_\perp) = \int d^3r \rho_J^*(r) = J^*(0) = \frac{1}{2}, \tag{36}$$

which provides a self-consistency check. As in the case of the mass distributions, both the 3D and 2D distributions for the angular momentum become broader as the nuclear density increases. It implies that the mean square radii of the angular momentum distribution also increase in nuclear matter (see also Table 1). The 3D distribution is broader than the 2D one. The factor $4/5$ in Eq. (11) arises again from the geometrical difference between the 3D and 2D angular-momentum distributions. The sign of each contribution is not changed after the Abel transformation. As shown in Eq. (8), $\rho_J^{(2D)}(x_\perp)$ is directly related to $\rho_J(r)$. As listed in Table 2, each contribution to the spin of the nucleon in nuclear matter is also changed. It is of great interest to see that the contribution of the kinetic term $\mathcal{L}_2^*$ is reduced in nuclear matter whereas that of the Skyrme term $\mathcal{L}_4^*$ is enhanced as the nuclear density increases. Nevertheless, the spin of the nucleon is always kept to be 1/2 as it should be.

4.3 Pressure and shear-force distributions of the nucleon

We are now in a position to discuss the pressure and shear-force distributions, which are crucial for the stability conditions of the nucleon. Figure 4 shows each contribution to the 3D and 2D pressure distributions multiplied by $4\pi r^2$ and $2\pi x_\perp$ in the upper and lower panels, respectively. We draw the 3D and 2D weighted pressure densities in free space (nuclear matter) in the upper-left (upper-right) and lower-left (lower-right) panels, respectively. In fact, the results for the 3D distributions were already discussed in Refs. [43,56]. Thus, we will concentrate in this work on how the 2D pressure distributions undergo modification in nuclear matter in comparison with the 3D ones. As shown in Fig. 4, the Abel transformation does not change the general feature of each contribution. It means that the conclusions drawn in Refs. [43,56] are unchanged also in the 2D pressure distributions. The kinetic $\mathcal{L}_2^*$ and mass $\mathcal{L}_m^*$ terms of the pion provide the attractive force, whereas the Skyrme term $\mathcal{L}_4^*$ yields the repulsive force so that the stability of the nucleon is acquired. The pressure distribution should have at least one nodal point such that the global stability condition or the von Laue condition given in Eq. (14) is satisfied. It is achieved by the perfect balance between the kinetic $\mathcal{L}_2^*$ and mass $\mathcal{L}_m^*$ terms and the Skyrme $\mathcal{L}_4^*$ term. In the case of the 2D pressure distribution, we have the same conclusion. As listed in Table 2, the contributions of the kinetic $\mathcal{L}_2^*$ term to the 3D and 2D pressures decrease with the nuclear density increased, whereas the absolute magnitudes of the Skyrme $\mathcal{L}_4^*$ and mass $\mathcal{L}_m^*$ terms are enhanced in nuclear matter.

In Fig. 5, we depict the 3D and 2D pressure distributions of the nucleon as functions of the nuclear density ρ, multiplied by $4\pi r^2$ and $2\pi x_\perp$, respectively. The results show clearly that as ρ increases, both the 3D and 2D pressure distributions become broader. It implies that the nucleon swells in nuclear matter. If ρ continuously increases to higher densities, the negative pressure distribution of the kinetic term $\mathcal{L}_2^*$ gets further shallowed, which ends up with the situation that at a certain nuclear density the contribution of the kinetic term $\mathcal{L}_2^*$ will no more compensate that of the Skyrme term $\mathcal{L}_4^*$. As a result, there is no topological solution; the skyrmion disappears (for more discussion, we refer to Ref. [43]). It indicates that the nucleon may dissolve in quark matter.

The numerical value of $D(0)$ is obtained by integrating the 3D and 2D pressure distributions with the weights mr^2 and $4mx_\perp^2$ as shown in Eq. (19). The weights amplify the pressure distributions as r and $x_\perp$ increase. Thus, the negative tails of both $4\pi r^2 p^*(r)$ and $2\pi x_\perp \mathcal{P}^*(x_\perp)$ overwhelm the core parts so that the negative value of $D(0)$ is ensured. It implies that the correct balance of the pressure distributions is required to get the negative values of the D-term. In Table 2, we list the results for the D-term in the fourth column.

Figure 6 represents each contribution to the 3D and 2D shear-force distributions of the nucleon multiplied by $4\pi r^2$ and $2\pi x_\perp$ in the upper and lower panels, respectively. We want to mention that the mass term $\mathcal{L}_m^*$ does not contribute to the shear-force distribution as shown in Eq. (30). The general feature of each contribution is again well kept after the Abel transformation. In the case of the shear-force distributions, the contribution of the kinetic term $\mathcal{L}_2^*$ is generally dominant over that of the Skyrme term $\mathcal{L}_4^*$. As shown in Eq. (8), $S^*(x_\perp)$ is directly related to $s^*(r)$, so that the shapes of the 3D shear-force distributions are maintained by the Abel transformation. Since both the 3D (2D) shear-force distributions are positive over the whole ranges of r ($x_\perp$), the negative value of the D-term is also secured by Eq. (19).

In Fig. 7, we draw the 3D and 2D shear-force distributions of the nucleon as functions of the nuclear density ρ, multiplied by $4\pi r^2$ and $2\pi x_\perp$, respectively. Being similar to the case of the pressure distributions, both the 3D and 2D shear-force distributions get broadened as ρ increases. Considering the dependence of both the pressure and shear-force distributions on the nuclear density, we can easily understand the reason why the 3D and 2D mechanical radii become larger in nuclear matter than in free space. The 3D and 2D mechanical radii are defined in Eq. (17) in terms of the pressure and shear-force distributions. Since they get more extended in nuclear

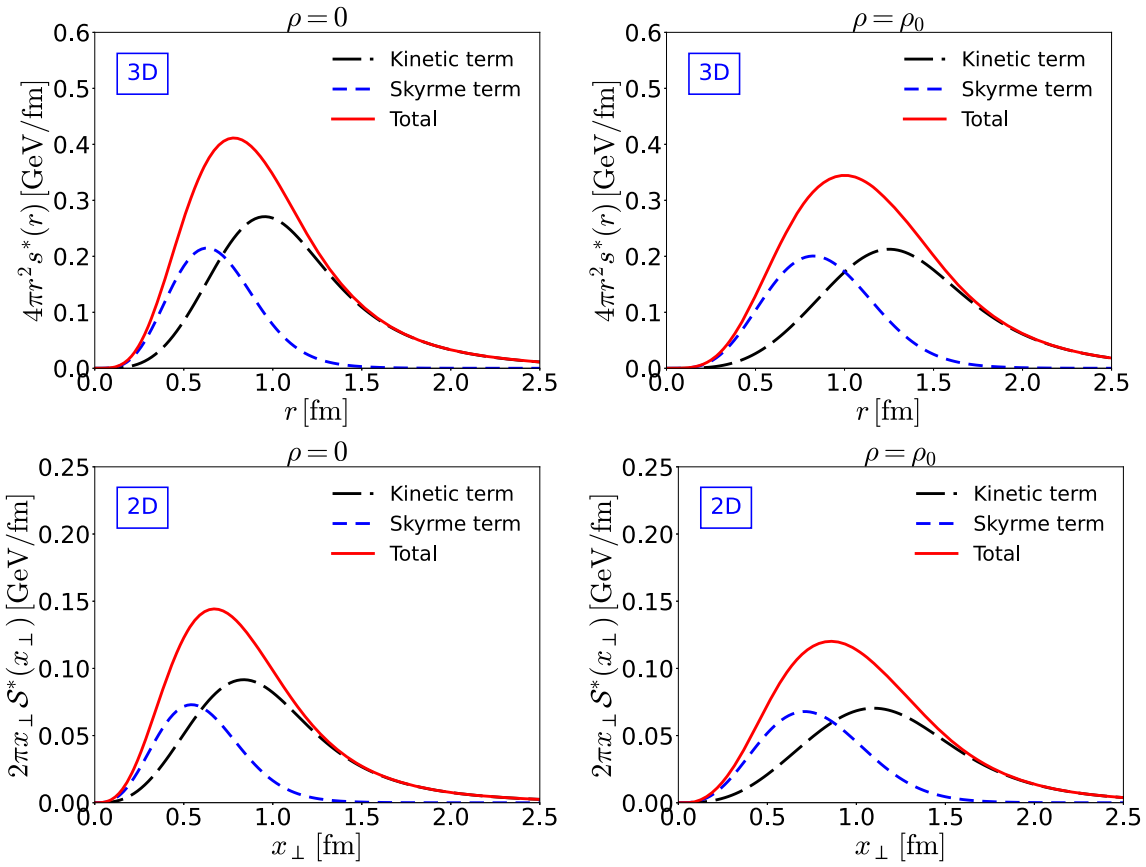

Fig. 6 3D and 2D shear-force distributions of the nucleon. The upper left (right) panel depicts the 3D shear-force distributions multiplied by $4\pi r^2$ at $\rho = 0$ ($\rho = \rho_0$). The lower left (right) panel draws the 2D shear-force distributions with $2\pi x_\perp$ at $\rho = 0$ ($\rho = \rho_0$). Notations are the same as in Fig. 2

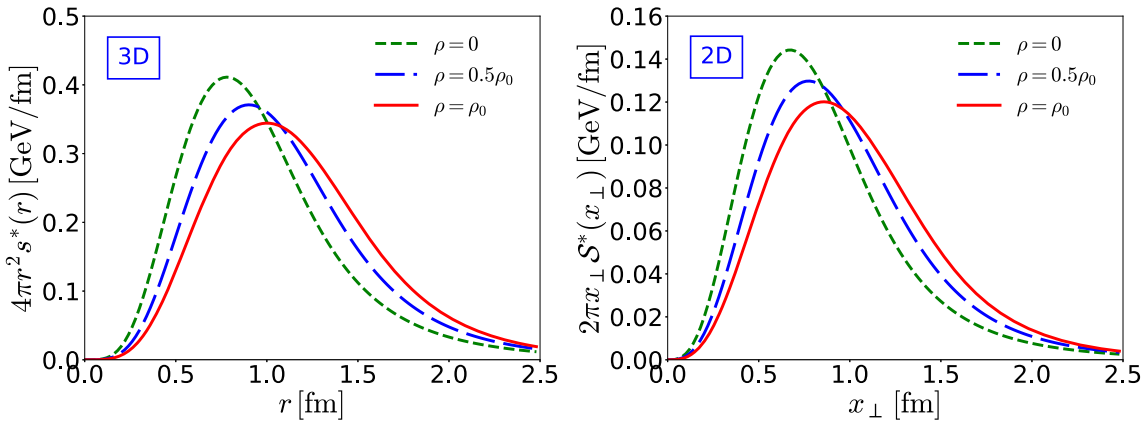

Fig. 7 3D and 2D pressure distributions of the nucleon as functions of the nuclear density ρ, multiplied by $4\pi r^2$ and $2\pi x_\perp$, respectively. Notations are the same as in Fig. 5

matter, the mechanical radii become larger as ρ increases, as shown in Table 1. Its physical implication is crucial because the mechanical radius of the nucleon exhibits the physical size of the nucleon. The results for the mechanical radii indicate that the nucleon swells in nuclear matter. It also implies that the local stability condition in Eq. (16) is satisfied. Its positivity is indeed kept intact also in nuclear matter.

It is of great interest to examine the ordering of the magnitudes of the nucleon radii as done in Ref. [36]. Table 1 displays the following ordering for the 3D and 2D radii:

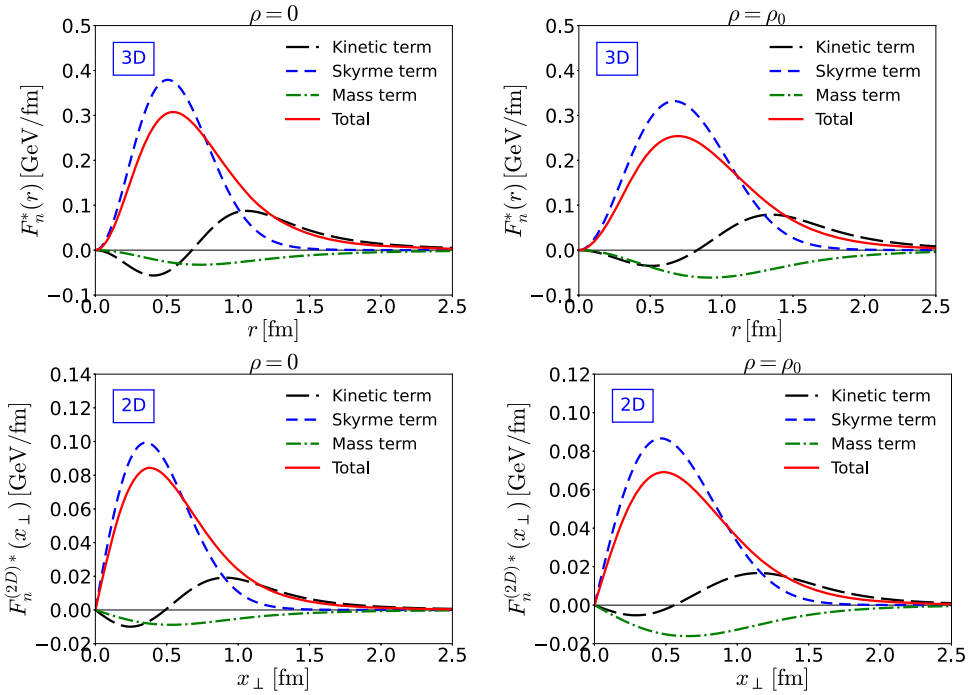

Fig. 8 3D and 2D normal force fields inside the nucleon. The upper-left (-right) panel depicts the 3D normal force field at $\rho = 0$ ($\rho = \rho_0$). The lower-left (-right) panel draws the 2D force normal force fields at $\rho = 0$ ($\rho = \rho_0$). Notations are the same as in Fig. 2

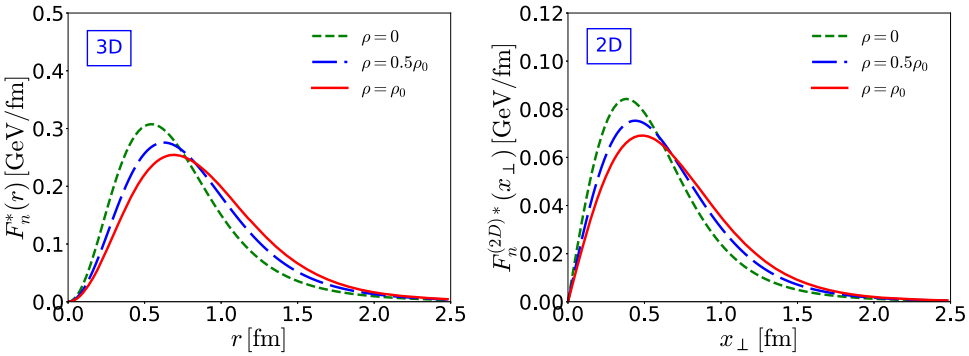

Fig. 9 3D and 2D normal force fields inside the nucleon as functions of the nuclear density ρ. The short-dashed, long-dashed, and solid curves represent the normal force fields with $\rho = 0,\ 0.5\rho_0,\ \rho_0$, respectively. ρ_0 denotes the normal nuclear matter density

$$\begin{aligned} &\langle x_\perp^2\rangle_{\mathcal{E}} < \langle x_\perp^2\rangle_{\rm mech} < \langle x_\perp^2\rangle_J \quad \text{(2D radii)},\\ &\langle r^2\rangle_{\mathcal{E}} < \langle r^2\rangle_{\rm mech} < \langle r^2\rangle_J \quad \text{(3D radii)}. \end{aligned} \tag{37}$$

While the ordering of the 2D radii is in agreement with that in the chiral quark-soliton model [36], the 3D radii are ordered differently. We have the same orderings in nuclear matter.

4.4 3D and 2D force fields inside the nucleon

The strong force fields inside a nucleon reveal how the nucleon acquires stability microscopically. As derived in Eq. (18), the normal and tangential force fields inside the nucleon are nothing but the stability conditions given in Eqs. (16) and (15): the 3D and 2D normal force fields should be positive over the whole ranges, and the tangential force fields should have at least one nodal point to secure the stability condition. Figure 8 illustrates how the normal force field satisfies the local stability condition. As shown in the upper-left panel of Fig. 8, the positivity of $F_n(r)$ is achieved in a nontrivial way. The Skyrme term $\mathcal{L}_4^*$ plays an essential role in making $F_n(r)$ satisfy the local stability condition. Interestingly, the stable topological soliton arises when the Skyrme term $\mathcal{L}_4^*$ is included. It is noticeable that this characteristic of the Skyrme model is reflected in the local stability condition. On the other hand, the kinetic term $\mathcal{L}_2^*$ negatively contributes to the core part but positively to the outer shell. The mass term $\mathcal{L}_m^*$ always provides a negative contribution. The lower-left panel of Fig. 8 shows that the Abel transformation does not change the main feature of each contribution. As shown in the right panels of Fig. 8, both the 3D and 2D normal force fields become broadened in nuclear matter. Figure 9 exhibits how the normal force fields undergo this broadening as ρ increases.

The upper-left panel of Fig. 10 reminds us of the pressure distributions in Fig. 4. The tangential force field is just the integrand of the global stability condition or the von Laue

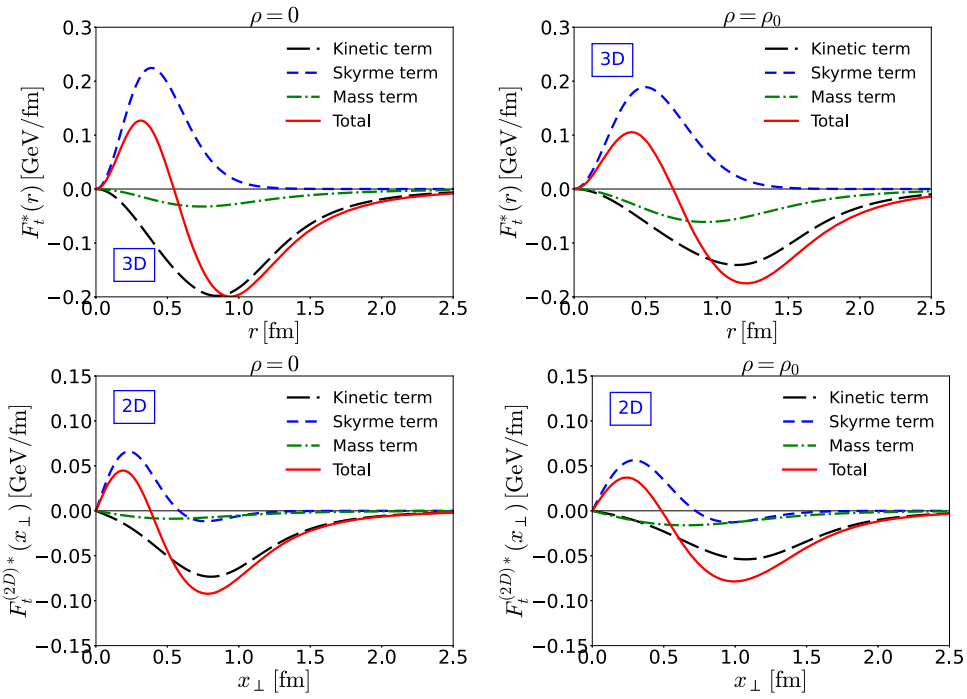

Fig. 10 3D and 2D tangential force fields inside the nucleon. The upper-left (-right) panel depicts the 3D normal tangential field at $\rho = 0$ ($\rho = \rho_0$). The lower-left (-right) panel draws the 2D force tangential force fields at $\rho = 0$ ($\rho = \rho_0$). Notations are the same as in Fig. 2

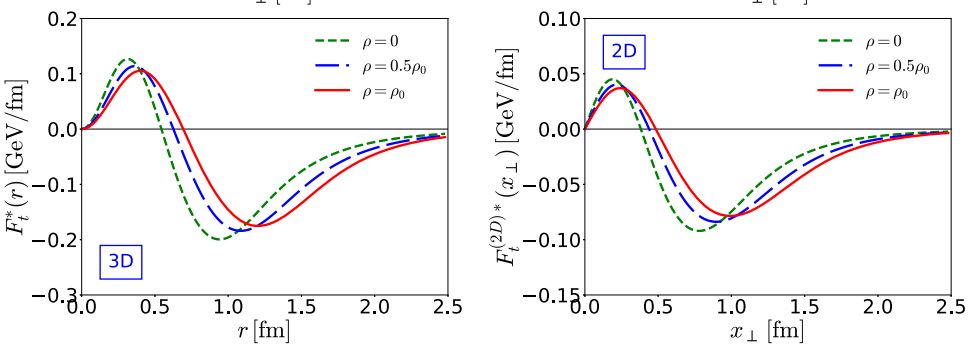

Fig. 11 3D and 2D tangential force fields inside the nucleon as functions of the nuclear density ρ. The short-dashed, long-dashed, and solid curves represent the tangential force fields with $\rho = 0,\ 0.5\rho_0,\ \rho_0$, respectively. ρ_0 denotes the normal nuclear matter density

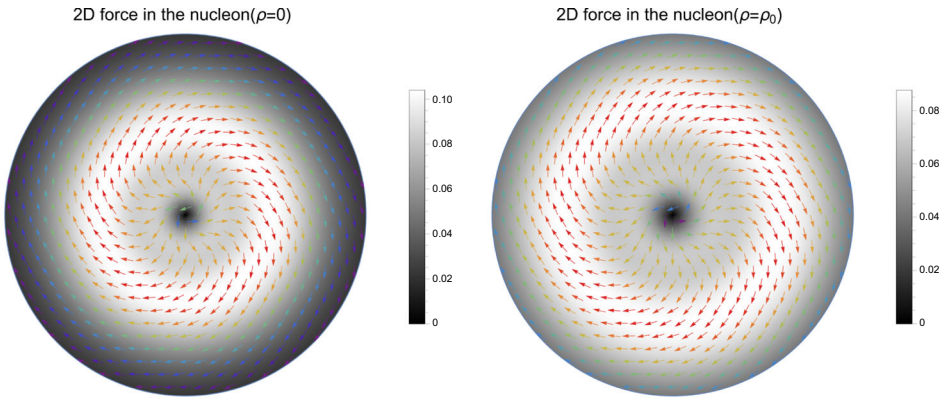

Fig. 12 Visualization of the 2D strong force field inside the nucleon. The left panel illustrates that in free space, whereas the right panel displays that in nuclear matter at the normal nuclear matter density

condition as shown in Eq. (15). Thus, the role of each contribution is the same as in the case of the pressure distributions as revealed in the upper-left panel of Fig. 10. It is kept unmarred after the Abel transformation, as shown in the lower-left panel of Fig. 10. Figure 11 demonstrates convincingly that the tangential force fields also get broadened as ρ increases. Note that the sign of the 2D tangential force field turns negative at around $x_\perp \approx 0.39$ fm in free space whereas at around $x_\perp \approx 0.48$ fm at $\rho = \rho_0$.

The total strong force field in free space (nuclear matter) is visualized in the left (right) panel of Fig. 12. The core part of the strong force field is dominated by the normal force field, whereas the outer shell is governed by the tangential one. This behavior of the strong force field ensures that the nucleon acquires stability. In Ref. [62], it was shown that $F_t(x_\perp)$ comes into leading play at large distances in a model-independent way if one uses the r dependence of the pressure and shear-force distributions. Last but not least, we want to mention that the total internal force fields include also contributions from the opposite direction to the force fields drawn in Fig. 12. So, the nucleon is kept to be static.

5 Summary and outlook

In the present work, we aimed at investigating the gravitational form factors of the nucleon and the corresponding mechanical distributions in nuclear matter within the framework of the in-medium modified Skyrme model. We first computed the three different gravitation form factors of the nucleon: the mass, angular momentum, and D-term form factors with the nuclear density varied from $\rho = 0$ to $\rho = \rho_0$, where ρ_0 denotes the normal nuclear matter density. As the momentum transfer increases, the mass and angular momentum form factors fall off faster than the case in free space with ρ increased. Since they are normalized to $A^*(0) = 1$ and $J^*(0) = 1/2$, the magnitudes of these two form factors at $t = 0$ are not changed. On the other hand, the absolute magnitude of the D-term form factor is enhanced in nuclear matter and drops off more rapidly than in free space. We then examined the mass distribution of the nucleon in nuclear matter. Each contribution of the kinetic term, the Skyrme term, and the mass term becomes broader as ρ increases. This feature is kept unchanged by the Abel transformation except for the mass term. The contribution of the mass term turns negative in the two-dimensional transverse plane on the light cone. The angular momentum distributions show similar behaviors as the nuclear density is changed.

The pressure and shear-force distributions play crucial roles in understanding the stability of the nucleon. The pressure distribution has at least one nodal point so that the von Laue condition is satisfied. The kinetic term and mass term of the pion provide attraction whereas the Skyrme term yields repulsion. As the nuclear density increases, both the 3D and 2D pressure distributions becomes broader. The shear-force distributions exhibit the density dependence, being similar to the pressure distributions. The Abel transformations do not change the general features of the pressure and shear-force distributions. The local and global stability conditions are satisfied also in nuclear matter. The mass, angular momentum, and mechanical radii of the nucleon become larger in nuclear matter than in free space, which indicates that the nucleon swells in nuclear matter.

Finally, we scrutinized the strong normal and tangential force fields, which are deeply related to the stability conditions. The normal force fields are positive over the whole space and transverse plane. The 2D strong force fields keep all important features of the 3D force fields, which means that the Abel transformation does not change the characteristics of the force fields. In conclusion, the nucleon acquires stability also in nuclear matter in a certain range of the nuclear matter density.

Acknowledgements The work was supported by the Deutscher Akademischer Austauschdienst (DAAD) doctoral scholarship (J.-Y.K) and Basic Science Research Program through the National Research Foundation of Korea funded by the Korean government (Ministry of Education, Science and Technology, MEST), Grant-no. 2020R1F1A1067876 (U. Y.) and 2021R1A2C2093368, 2018R1A 5A1025563 (H.-Ch.K.).

Data Availability Statement This manuscript has no associated data or the data will not be deposited. [Authors' comment: Since the present work is a theoretical one, we do not have deposited data. We have only the theoretical results presented already in the manuscript.]

Funded by SCOAP[3]. SCOAP[3] supports the goals of the International Year of Basic Sciences for Sustainable Development.

References

1. I.Y. Kobzarev, L.B. Okun, Zh. Eksp, Zh. Eksp. Teor. Fiz. **43**, 1904 (1962)
2. H. Pagels, Phys. Rev. **144**, 1250 (1966)
3. D. Müller, D. Robaschik, B. Geyer, F.M. Dittes, J. Hořejši, Fortschr. Phys. **42**, 101 (1994). arXiv:hep-ph/9812448
4. X.D. Ji, Phys. Rev. Lett. **78**, 610 (1997). arXiv:hep-ph/9603249
5. A.V. Radyushkin, Phys. Lett. B **380**, 417 (1996). arXiv:hep-ph/9604317

6. K. Goeke, M.V. Polyakov, M. Vanderhaeghen, Prog. Part. Nucl. Phys. **47**, 401 (2001). arXiv:hep-ph/0106012
7. M. Diehl, Phys. Rep. **388**, 41 (2003). arXiv:hep-ph/0307382
8. A.V. Belitsky, A.V. Radyushkin, Phys. Rep. **418**, 1 (2005). arXiv:hep-ph/0504030
9. V.D. Burkert, L. Elouadrhiri, F.X. Girod, Nature **557**, 396 (2018)
10. K. Kumerički, Nature **570**(7759), E1–E2 (2019)
11. H. Dutrieux, C. Lorcé, H. Moutarde, P. Sznajder, A. Trawiński, J. Wagner, Eur. Phys. J. C **81**(4), 300 (2021). arXiv:2101.03855 [hep-ph]
12. V.D. Burkert, L. Elouadrhiri, F.X. Girod, arXiv:2104.02031 [nucl-ex]
13. M. Laue, Ann. Phys. **340**, 524 (1911)
14. M.V. Polyakov, P. Schweitzer, Int. J. Mod. Phys. A **33**, 1830025 (2018). arXiv:1805.06596 [hep-ph]
15. M.V. Polyakov, Phys. Lett. B **555**, 57 (2003). arXiv:hep-ph/0210165
16. C. Lorcé, H. Moutarde, A.P. Trawiński, Eur. Phys. J. C **79**, 89 (2019). arXiv:1810.09837 [hep-ph]
17. K. Goeke, J. Grabis, J. Ossmann, M.V. Polyakov, P. Schweitzer, A. Silva, D. Urbano, Phys. Rev. D **75**, 094021 (2007). arXiv:hep-ph/0702030
18. D.R. Yennie, M.M. Levy, D.G. Ravenhall, Rev. Mod. Phys. **29**, 144 (1957)
19. M. Burkardt, Phys. Rev. D **62**, 071503 (2000). [Erratum: Phys. Rev. D **66**, 119903 (2002)]. arXiv:hep-ph/0005108
20. M. Burkardt, Int. J. Mod. Phys. A **18**, 173 (2003). arXiv:hep-ph/0207047
21. G.A. Miller, Phys. Rev. Lett. **99**, 112001 (2007). arXiv:0705.2409 [nucl-th]
22. G.A. Miller, Annu. Rev. Nucl. Part. Sci. **60**, 1 (2010)
23. R.L. Jaffe, Phys. Rev. D **103**, 016017 (2021). arXiv:2010.15887 [hep-ph]
24. R. Hofstadter, Rev. Mod. Phys. **28**, 214 (1956)
25. R. Hofstadter, Annu. Rev. Nucl. Part. Sci. **7**, 231 (1957)
26. C. Lorcé, L. Mantovani, B. Pasquini, Phys. Lett. B **776**, 38 (2018). arXiv:1704.08557 [hep-ph]
27. C. Lorcé, Eur. Phys. J. C **78**, 785 (2018). arXiv:1805.05284 [hep-ph]
28. C. Lorcé, Phys. Rev. Lett. **125**, 232002 (2020). arXiv:2007.05318 [hep-ph]
29. C. Lorcé, Eur. Phys. J. C **81**, 413 (2021). arXiv:2103.10100 [hep-ph]
30. E.P. Wigner, Phys. Rev. **40**, 749–760 (1932)
31. M. Hillery, R.F. O'Connell, M.O. Scully, E.P. Wigner, Phys. Rep. **106**, 121 (1984)
32. C.E. Carlson, M. Vanderhaeghen, Phys. Rev. Lett. **100**, 032004 (2008). arXiv:0710.0835 [hep-ph]
33. J.Y. Kim, H.-Ch. Kim, Phys. Rev. D **104**, 074003 (2021). arXiv:2106.10986 [hep-ph]
34. C. Lorcé, P. Wang, Phys. Rev. D **105**, 096032 (2022). https://doi.org/10.1103/PhysRevD.105.096032. arXiv:2204.01465 [hep-ph]
35. J.Y. Panteleeva, M.V. Polyakov, Phys. Rev. D **104**, 014008 (2021). arXiv:2102.10902 [hep-ph]
36. J.Y. Kim, H.-Ch. Kim, Phys. Rev. D **104**, 074019 (2021). arXiv:2105.10279 [hep-ph]
37. J.Y. Kim, Phys. Rev. D **106**, 014022 (2022). https://doi.org/10.1103/PhysRevD.106.014022. arXiv:2204.08248 [hep-ph]
38. N.H. Abel, J. Reine Angew. Math. **1**, 153 (1826)
39. F. Natterer, *The Mathematics of Computerized Tomography* (Wiley, New York, 2001)
40. M.V. Polyakov, Phys. Lett. B **659**, 542 (2008). arXiv:0707.2509 [hep-ph]
41. A.M. Moiseeva, M.V. Polyakov, Nucl. Phys. B **832**, 241 (2010). arXiv:0803.1777 [hep-ph]
42. A. Freese, G.A. Miller, Phys. Rev. D **105**, 014003 (2022). arXiv:2108.03301 [hep-ph]
43. H.-Ch. Kim, P. Schweitzer, U. Yakhshiev, Phys. Lett. B **718**, 625 (2012). arXiv:1205.52275 [hep-ph]
44. A. Rakhimov, M.M. Musakhanov, F.C. Khanna, U.T. Yakhshiev, Phys. Rev. C **58**, 1738 (1998). arXiv:nucl-th/9609049
45. A.M. Rakhimov, F.C. Khanna, U.T. Yakhshiev, M.M. Musakhanov, Nucl. Phys. A **643**, 383 (1998). arXiv:nucl-th/9806062
46. G.S. Adkins, C.R. Nappi, E. Witten, Nucl. Phys. B **228**, 552 (1983)
47. U. Yakhshiev, H.-Ch. Kim, Phys. Rev. C **83**, 038203 (2011). arXiv:1009.2909 [hep-ph]
48. M.V. Polyakov, P. Schweitzer, PoS SPIN **2018**, 066 (2019). arXiv:1812.06143 [hep-ph]
49. J.Y. Kim, B.D. Sun, Eur. Phys. J. C **81**, 85 (2021). arXiv:2011.00292 [hep-ph]
50. E. Epelbaum, J. Gegelia, N. Lange, U.G. Meißner, M.V. Polyakov, Phys. Rev. Lett. **129**, 012001 (2022). https://doi.org/10.1103/PhysRevLett.129.012001. arXiv:2201.02565 [hep-ph]
51. P. Schweitzer, K. Tezgin, Phys. Lett. B **796**, 47 (2019)
52. A. Freese, G.A. Miller, Phys. Rev. D **103**, 094023 (2021). arXiv:2102.01683 [hep-ph]
53. C. Lorcé, P. Schweitzer, K. Tezgin, Phys. Rev. D **106**, 1 (2022). https://doi.org/10.1103/PhysRevD.106.014012. arXiv:2202.01192 [hep-ph]
54. J.Y. Kim, H.-Ch. Kim, M.V. Polyakov, H.D. Son, Phys. Rev. D **103**, 014015 (2021). arXiv:2008.06652 [hep-ph]
55. I.A. Perevalova, M.V. Polyakov, P. Schweitzer, Phys. Rev. D **94**, 054024 (2016). arXiv:1607.07008 [hep-ph]
56. C. Cebulla, K. Goeke, J. Ossmann, P. Schweitzer, Nucl. Phys. A **794**, 87 (2007). arXiv:hep-ph/0703025
57. K. Kumerički, D. Müller, EPJ Web Conf. **112**, 01012 (2016). arXiv:1512.09014 [hep-ph]
58. X.D. Ji, W. Melnitchouk, X. Song, Phys. Rev. D **56**, 5511 (1997). arXiv:hep-ph/9702379
59. B. Pasquini, M.V. Polyakov, M. Vanderhaeghen, Phys. Lett. B **739**, 133 (2014). arXiv:1407.5960 [hep-ph]
60. P. Hagler et al. (LHPC), Phys. Rev. D **77**, 094502 (2008). arXiv:0705.4295 [hep-lat]
61. V. Guzey, M. Siddikov, J. Phys. G **32**, 251 (2006). arXiv:hep-ph/0509158
62. H. Alharazin, D. Djukanovic, J. Gegelia, M.V. Polyakov, Phys. Rev. D **102**, 076023 (2020). arXiv:2006.05890 [hep-ph]